Original papers

Wheat yellow rust monitoring by learning from multispectral UAV aerial imagery

Jinya Su[a,*], Cunjia Liu[a], Matthew Coombes[a], Xiaoping Hu[b,*], Conghao Wang[b], Xiangming Xu[c], Qingdong Li[d], Lei Guo[d], Wen-Hua Chen[a]

[a] Department of Aeronautical and Automotive Engineering, Loughborough University, Loughborough LE11 3TU, UK
[b] State Key Laboratory of Crop Stress Biology for Arid Areas, College of Plant Protection, Northwest A&F University, Yangling, China
[c] NIAB EMR, Genetics and Crop Improvement, East Malling Research, West Malling ME19 6BJ, UK
[d] School of Electrical Engineering and Automation, Beihang University, Beijing 100191, China

ARTICLE INFO

ABSTRACT

The use of a low-cost five-band multispectral camera (RedEdge, MicaSense, USA) and a low-altitude airborne platform is investigated for the detection of plant stress caused by yellow rust disease in winter wheat for sustainable agriculture. The research is mainly focused on: (i) determining whether or not healthy and yellow rust infected wheat plants can be discriminated; (ii) selecting spectral band and Spectral Vegetation Index (SVI) with a strong discriminating capability; (iii) developing a low-cost yellow rust monitoring system for use at farmland scales. An experiment was carefully designed by infecting winter wheat with different levels of yellow rust inoculum, where aerial multispectral images under different developmental stages of yellow rust were captured by an Unmanned Aerial Vehicle at an altitude of 16–24 m with a ground resolution of 1–1.5 cm/pixel. An automated yellow rust detection system is developed by learning (via random forest classifier) from labelled UAV aerial multispectral imagery. Experimental results indicate that: (i) good classification performance (with an average Precision, Recall and Accuracy of 89.2%, 89.4% and 89.3%) was achieved by the developed yellow rust monitoring at a diseased stage (45 days after inoculation); (ii) the top three SVIs for separating healthy and yellow rust infected wheat plants are RVI, NDVI and OSAVI; while the top two spectral bands are NIR and Red. The learnt system was also applied to the whole farmland of interest with a promising monitoring result. It is anticipated that this study by seamlessly integrating low-cost multispectral camera, low-altitude UAV platform and machine learning techniques paves the way for yellow rust monitoring at farmland scales.

1. Introduction

Agricultural crops are usually threatened by multiple pests and diseases (e.g. yellow rust, powdery mildew, aphid) causing significant economic losses (Yuan et al., 2014). A common disease control method is calendar-based application of pesticides irrespective of current disease development and risks. Such a control strategy, however, not only incurs a high cost (economically) but also increases the likelihood of ground water contamination (environmentally) and pesticide residues in agriculture products (socially) (Moshou et al., 2004). Therefore, there is a trend to adopt a decision-based disease management strategy in which automated non-destructive plant disease detection/quantification plays an important role, enabling site-specific disease control (Sankaran et al., 2010).

It is highly desirable that the detection/quantification method is rapid, specific to a particular disease, and sensitive for detection at an early onset of the symptoms (López et al., 2003). Spectroscopic imaging provides a promising solution for a large-scale disease monitoring under field conditions and is receiving ever-increasing research interests (Zhang and Kovacs, 2012). Various types of sensors are available to measure the amount of reflected solar radiation: from low-cost multispectral to high-cost imaging spectrometers, from low spatial to high spatial resolution, and from ground-based to aircraft or even satellite-based (Hunt et al., 2013).

Generally speaking, crop diseases cause certain typical changes in reflection behaviour of plants. For instance, pathogens cause a reduction of plant ChlorophyII content in the VISible (VIS) and RedEdge region of the spectrum (550 nm; 650–720 nm) due to necrotic or

chlogotic lesions (Franke et al., 2005). Browning effects by senescence of infected plant tissues affect the VIS and near-infrared (NIR) (680–800 nm) as well as short-wave infrared (SWIR) regions (1400–1600 nm and 1900–2100 nm) due to dryness. Therefore, reflectance differences between healthy and diseased plant tissues can be captured by spectroscopic imaging and consequently be learnt by advanced machine learning algorithms.

This work is focused on the detection of yellow rust on winter wheat with UAV multispectral imagery and state-of-the-art machine learning algorithms. Yellow rust is caused by *Puccinia striiformis f. sp. Tritici (Pst)*, which produces yellow coloured spores on leaves. This disease is also called stripe rust, since chlorosis generally occurs in a narrow stripe, 2 or 3 mm wide and running parallel to the leaf veins (Moshou et al., 2004). Yellow rust is a destructive disease affecting wheat production worldwide and may result in a severe yield loss (Zhang et al., 2012). Yellow rust development is affected by many factors (i.e. meteorological conditions) (Pavli et al., 2011). An accurate detection/quantification of its occurrence is of high importance for sustainable management (Zhang et al., 2012).

A number of pioneering studies on yellow rust disease detection are available in the literature, although most of them focused on leaf scale (or ground level, or 'near target'scale). Hyperspectral images (410–910 nm) were evaluated for leaf rust detection in greenhouse at an altitude of 1.75 m, where decision tree analysis discovered that leaf rust could be detected five days after inoculation (Franke et al., 2005). In-field spectral images were taken by a spectrograph (460–900 nm) mounted at spray boom level in Moshou et al. (2004), 543 nm (Green), 630 nm, 750 nm and 861 nm (NIR) were found to be the most discriminating wavelengths. Spectrophotometer (450–1000 nm) was used to evaluate the classification ability of 22 narrow-band Spectral Vegetation Indices (SVIs) (Ashourloo et al., 2014), where the top three are Narrow-band Normalized Difference Vegetation Index (NDVI) (Rouse et al., 1974; Tucker, 1979), Green Index (GI) (Zarco-Tejada et al., 2005) and Anthocyanin Reflectance Index (ARI) (Gitelson et al., 2001). Ten SVIs were used to discriminate leaf yellow (stripe) and stem rust by spectrophotometer (450–900 nm) (Devadas et al., 2009), where ARI and Transformed ChlorophyII Absorption and Reflectance Index (TCARI) (Haboudane et al., 2002) were identified to be the best SVIs. Recently, Yellow Rust Index (YRI) was also developed for wheat yellow rust on the basis of hyperspectral wavelength ranking using RELIEF-F algorithm (Huang et al., 2014). Hyperspectral image has also been used to discriminate yellow rust, powdery mildew and wheat aphid (Yuan et al., 2014), and yellow rust from nutrient stress (Zhang et al., 2012). Recently, wavelet spectral features were proved to be more effective than conventional nine SVIs for leaf yellow rust using spectrometer (350–2500 nm) (Zhang et al., 2014).

It should be noted that ground level yellow rust detection is very valuable for wavelength selection and SVI analysis, however, remote sensing data validation is highly desirable and necessary for practical applications at farmland (small) scales. This is because the substantially reduced spatial resolution of remote sensing image will generally bring new challenges such as the problem of mixed pixels. In comparison to the detection of leaf yellow rust, there is very limited published information on airborne or satellite remote sensing for yellow rust. A noteworthy work was (Huang et al., 2007), where airborne hyperspectral imaging was adopted for wheat yellow rust identification. In this work, regression analysis was conducted to demonstrate that Photochemical Reflectance Index, $PRI = (R-531-R_{570})/(R-531+R_{570})$, was an effective index (i.e. with a high coefficient of determination) for yellow rust disease severities. Satellite remote sensing has also been considered for large scale monitoring of yellow rust (Zhang et al., 2011; Yuan et al., 2017). It should also be noted that airborne or satellite based remote sensing, although promising for large-scale applications, is usually limited by their high operational complexity, cost and lengthy delivery of products and therefore not suitable for use at farmland (small) scales (Zhang and Kovacs, 2012).

With user-defined spatial–temporal resolution, low cost and flexibility, UAV based remote sensing (equipped with red-green–blue (RGB), multispectral, hyperspectral and thermal cameras, and radar, etc.) is gathering ever-increasing research interest, and has become an important complement for satellite and aircraft based remote sensing (Zhang and Kovacs, 2012). In the past decades, UAV remote sensing has been adopted for various precision agriculture applications including crop classification, estimation of agronomic parameters (e.g. leaf area index, biomass (Yue et al., 2017), nitrogen content, plant density (Jin et al., 2017)), disaster monitoring (e.g. pest, disease, lodging (Liu et al., 2018) and water stress (Bellvert et al., 2014; Romero et al., 2018; Su et al., 2018)), among many others. To summarize, the following observations are presented.

(1) There is an urgent need for yellow rust monitoring system to enable site-specific disease management;
(2) Extensive studies are available on leaf-scale yellow rust detection using hyperspectral image, but little work is available on the use of low-cost, high-resolution and user-friendly multispectral image for yellow rust research at larger scales;
(3) Airborne/satellite remote sensing is suitable for large scale applications, however, may not be suitable for use at farmland scales due to its low spatial resolution and high operating cost and complexity;
(4) UAV remote sensing has been successfully used in many precision agriculture applications, however, its application (particular with state-of-the-art RedEdge multispectral camera) to yellow rust is yet to be fully exploited.

This work aims at evaluating the usefulness of five-band multispectral camera (RedEdge) and a low-altitude UAV platform for the automatic detection of wheat yellow rust. The specific objectives of this study are: (i) determining whether or not healthy and yellow rust infected wheat plants can be discriminated by applying machine learning algorithms to multispectral UAV imagery; (ii) selecting spectral band and SVI that best differentiate healthy and yellow rust infected wheat plants from available five bands and widely used SVIs; (iii) developing a low-cost and easily-deployed UAV remote sensing system for yellow rust monitoring at farmland scales.

2. Materials

In this section, materials related to this research are presented including field experiment setup for wheat yellow rust, UAV-Camera system for multispectral image acquisition, Pix4D software for image preprocessing (e.g. image calibration, stitching and SVI calculation).

2.1. Field yellow rust experiment setup

Experiments were carried out on Caoxinzhuang experimental filed (latitude: 34°306′N, longitude: 108°090′E, 499 m a.s.l.) of Northwest A&F University, Yangling, Shanxi Province, China (see, Fig. 1 for its geographic location). The region is of warm temperate semi-humid and semi-arid climate, where the mean annual temperature, rainfall and hours of sunshine are 12.9 °C, 635 mm (mostly in June-September) and 2164 h, respectively. The soil type is manured loessal soil with PH value of 8.0–8.8, with organic content of 8.0–15.0%, and with Nitrogen, Phosphorus and Kalium of 0.6–1.0%, 1.0–2.0%, 20%+, respectively. Xiaoyan 22, one wheat variety developed by Northwest A&F university in 1989, was chosen. Wheat seeds were sown with a row spacing of 16 cm and at a rate of 30 g seeds/m² on 05/October/2017. The field was irrigated twice on 10/December/2017 and 13/March/2018, respectively. In addition, no fertilizer was used.

In this study, the mixed *Pst* races (CYR 29, CYR 30, CYR 31, CYR 32, CYR 33) were used to inoculate wheat seedlings on 23/March/2018, where the inoculation method is standard and referred to Liu et al. (2018) for more detailed information. Six plots (including a healthy one
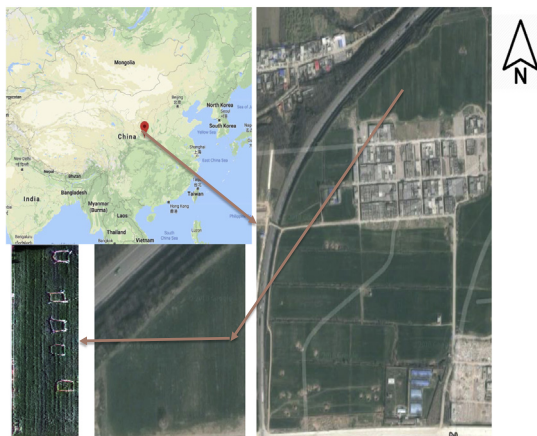
Fig. 1. Geographic location of the experimental wheat field.

for blank comparison), each 2 m× 2 m, each inoculated with one of the six levels of yellow rust inoculum (i.e. 0, 0.33 g, 0.67 g, 1.00 g, 1.33 g and 1.67 g from south to north) but not treated with any fungicide, were used to study disease development/spread and its detection by UAV multispectral image.

2.2. UAV-Camera system for multispectral imagery

In this work, a commercial aircraft DJI Spreading Wings S1000 Octocopter (DJI Company, Shenzhen, China) and a 5-band multispectral camera (RedEdge, MicaSense Inc., Seattle, USA), as displayed in Fig. 2, constitute a platform of low altitude UAV-camera system. The diameter, height, take-off weight and hovering time of DJI S1000 are 1045 mm, 386 mm, 6.0Kg–11.0Kg and 30 min, respectively (Su et al., 2018). The weight, dimensions, image resolution of RedEdge camera are 135 g, 5.9 cm × 4.1 cm × 3.0 cm and 1280 × 960 pixels, respectively. RedEdge camera, equipped with GPS, can capture five spectral images simultaneously, where the spectral information is displayed in Table 1.

Multispectral images were acquired on several key yellow rust developmental stages including inoculation date (23/March/2018), incubation stage (01/April/2018), early onset (17/April/2018) and diseased stages (02/May/2018 (no useful aerial images were obtained on this date due to a strong wind), 07/May/2018), respectively. In each flight, RedEdge camera was fixed on a gimbal, pointing vertically downwards to guarantee aerial image quality. Flight altitude was set at 16–24 meters above ground, providing images with a ground spatial resolution of 1–1.5 cm/pixel. A laptop installed with Ground Control Station was used to plan, monitor and control the UAV flight. The planned flight path and velocity, and camera triggering are designed so

Fig. 2. UAV-Camera system: DJI S1000 UAV (left), RedEdge camera (upper-right corner) and reflectance panel (lower-right corner).

Table 1
Spectral information of RedEdge camera.

Band No.	Name	Center Wavelength	Bandwidth	Panel reflectance
1	Blue	475 nm	20 nm	0.57
2	Green	560 nm	20 nm	0.57
3	Red	668 nm	10 nm	0.56
4	NIR	840 nm	40 nm	0.51
5	RedEdge	717 nm	10 nm	0.55

that the consecutive images with overlap and sidelap up to 75 % can be obtained for the purpose of accurate orthomosaic generation. An image of a reflectance calibration panel (see, lower-right corner of Fig. 2 for image and Table 1 for panel reflectance value) was always taken at about 1 m height immediately before and after each flight to account for camera characteristics, reflectance characteristics and the effects of environmental variations. Each UAV aerial image contains necessary information for camera calibration and image stitching such as camera information (e.g. exposure time, ISO speed, focal length, black level), GPS and IMU (i.e. Latitude, Longitude, Altitude, Yaw, Pitch and Roll).

2.3. Pix4D Mapper for image preprocessing

Image pre-processing to generate calibrated and georeferenced spectral reflectance and SVIs was performed by using commercial Pix4Dmapper software of version 4.2.27 (Educational Licence of 1500 EUR, Pix4D SA, Switzerland), which include initial processing (e.g. keypoint computation for image matching), orthomosaic generation and index calculation (with reflectance calibration). Each layer output (e.g. spectral reflectance for each band and various SVIs) is a single high-resolution GeoTIFF image of the whole site. GeoTIFF images were further post-processed in Matlab to define the common Region Of Interest (ROI) for various image layers so that follow-up analysis (e.g. spectral analysis and supervised classification) can be performed.

3. Systems and methods

Wheat plants under various levels of yellow rust infection generally have different spectral reflectance values. In this work, the problem of discriminating various wheat plants is formulated as a classification problem. Therefore, different elements for supervised classification are to be introduced such as data ground truthing, feature extraction, classifier selection and performance metric. In addition, to select spectral band and SVI that best differentiate healthy and yellow rust infected wheat plants, feature ranking algorithm is also adopted in this work. For the ease of understanding, the overall diagram of the developed yellow rust monitoring system is displayed in Fig. 3. The developed system in Fig. 3 contains classification model construction and application, where UAV-camera system is the shared block. In model construction, the collected aerial images for wheat field are first preprocessed by Pix4D software in Section 2.3, where features can be extracted including spectral bands and SVIs. Ground truth data is also collected from wheat field to label the image so that a labelled dataset is available for classifier training. Then random forest is adopted as the classifier, where its hyperparameters are fine tuned to guarantee satisfying performance by using Bayesian optimization. In model application to the FOI, the pre-processed aerial image by Pix4D can be classified by the trained classifier so that a yellow rust disease severity map can be generated. In the following subsections, different elements of the system are detailed.

3.1. Ground truth data

Ground truth labelling is indispensable in supervised learning (e.g. classification or regression). Ground truth data for wheat yellow rust severity was collected via visual inspection by experts of yellow rust
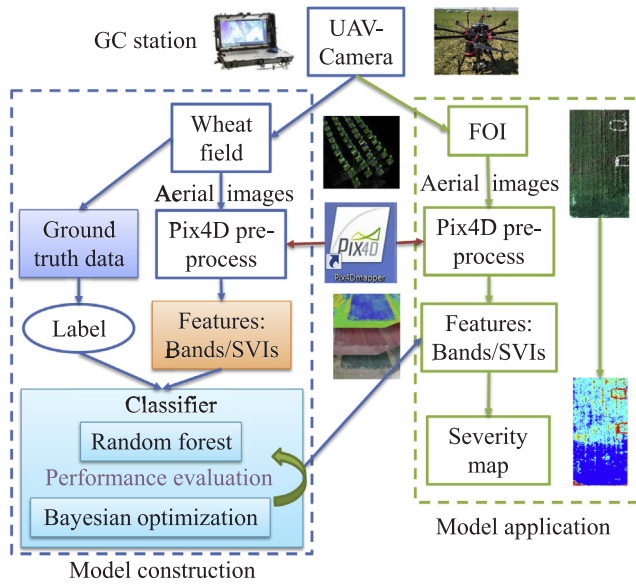
Fig. 3. The developed low-cost yellow rust UAV monitoring system for use at farmland scales: model construction (left part), model application for FOI (right part).

research. In particular, an intensive yellow rust severity was assessed on 17/April/2018 and 02/May/2018 for each wheat in the upper-left square of 1 m× 1 m for each 2 m× 2 m inoculated wheat square. For each wheat plant, yellow rust severity, the proportion of rust infected region over the whole wheat leaf, was assessed for top leaf, middle leaf and lower leaf, respectively following the yellow rust ground-truthing standard GB/T15795-2011 (Liu et al., 2018). For other UAV survey data, ground truth data was obtained by visual inspection of each inoculated wheat square/block due to a high workload involved in leaf based ground truthing. Ground truth data is to label aerial image, which in this work is to label different wheat squares so that a supervised classification model can be developed. After different severity labels are given to wheat squares, all wheat pixels within the squares are assumed to have the same yellow rust severity label. This approach is a common solution considering pixel level labelling is not possible for aerial image (Su et al., 2018).

3.2. Features: spectral bands and SVIs

Features, describing data characteristics, are of vital importance for machine learning applications, directly affecting algorithm performance. To maximally represent data characteristics, raw band reflectance and SVIs for wheat plants are considered concurrently for feature extraction. SVI is a simple but vital approach for extracting useful information from remotely sensed data, where most of them are calculated by using ratios or normalized difference of two or three bands (Hunt et al., 2013). SVIs have also been widely used to indirectly detect plant diseases in many preceding studies such as nitrogen monitoring (Ballester et al., 2017), yellow rust detection (Ashourloo et al., 2014). It is noted that different from SVIs for hyperspectral images, the SVIs for multispectral image are limited to the existing wide bands of the RedEdge camera. Therefore, on the basis of a detailed and careful literature survey, the adopted SVIs (totally 18) possibly related to yellow rust monitoring are summarized in Table 2.

3.3. Random forest classifier with Bayesian optimization

With feature vector and label being defined, the next step in classification tasks is to build a classifier from labelled data so that class label for new data can be automatically determined. A large number of

classification algorithms are available in the literature, where a suitable one for the task of interest is usually identified based on personal experience and trial & error experiments (Su et al., 2018). In this work, state-of-the-art random forest classifier is adopted due to its good performance in term of accuracy and robustness and a relatively low computation load, where its hyperparameters are automatically tuned by using Bayesian optimization.

Random forest is an ensemble learning based classifier. In this approach, a multitude of decision trees are constructed at training stage where the final class output is the mode of the classes of individual decision tree (Ho, 1995; Ho, 1998). In comparison to individual decision tree, Random forest has the fine property of avoiding overfitting to the training data and a better robustness. Certain hyperparameters exist in modern classification algorithms, which should be carefully tuned depending on different classification tasks (Thornton et al., 2013). To make this process automatic and efficient, Bayesian optimization is adopted (Snoek et al., 2012). To avoid distracting readers from the main contributions, Random forest classifier with Bayesian optimization is summarized in Algorithm 1, where interested readers are referred to Thornton et al. (2013) and Snoek et al. (2012) for more information.

Algorithm 1. Random Forest with Bayesian hyperparameter optimization

(a) **Parameter setting**: Set the number of decision trees in Random Forest, where a relatively large number (e.g. 150) can improve the algorithm robustness. Set certain stopping rules (e.g. evaluation number) to end the iteration.

(b) **Optimization problem**: Define hyperparameters to be optimized (e.g. minLS, numPTS) as $\lambda \in \Omega$, construct classification model with hyperparameters λ. Define the mean of the out-of-bag error (e.g. 'oobErr') as the objective function and the optimization problem is given by

$$\lambda_{opt} = \underset{\lambda \in \Omega}{\operatorname{argmin}}\, oobErr(\lambda). \tag{1}$$

(c) **Bayesian optimization**: Different from grid or random search, Bayesian optimization optimally suggests new parameters by sequentially performing: 1. fitting a Gaussian process model Q for data points $\{\lambda_i, oobErr(\lambda_i)\}$, and updating it with new data points; 2. finding new point for evaluation which maximizes the acquisition function based on the posterior distribution function Q. The introduction of acquisition function can efficiently trade off exploration and exploitation of parameter space.

(d) **Optimized classifier**: Stop evaluation when stopping criterion is satisfied and return the classifier with optimized hyperparameters.

3.4. Performance evaluation

Performance metrics are also introduced. In machine learning applications, True Positive (TP) is the correctly predicted positive values; False Positive (FP) denotes the scenario where actual class is negative and predicted class is positive; and False Negative (FN) represents the scenario that actual class is positive but predicted class is negative. From these parameters, a number of metrics can be defined for performance evaluation. In particular, Accuracy is a good measure for symmetric datasets (i.e. the number of each class has the same order of magnitude), given by

$$Accuracy = \frac{\sum TP}{All}. \tag{2}$$

Precision and Recall are also defined to effectively handle data with uneven class distribution. Following (Yi et al., 2017), these values are

Table 2
Spectral bands and SVIs adopted in this study.

Category (No.)	Name	Abbrev.	Band	Formula	Ref
Band(5)	Blue	–	Blue	R_b	–
	Green	–	Green	R_g	–
	Red	–	Red	R_r	–
	RedEdge	RE	RedEdge	R_{re}	–
	Near-infrared	NIR	NIR	R_{nir}	–
VIS(3)	Nitrogen Reflectance Index	NRI	Green–Red	$(R_g - R_r)/(R_g + R_r)$	Filella et al. (1995)
	Greenness Index	GI	Green–Red	R_g/R_r	Zarco-Tejada et al. (2005)
	Green Leaf Index	GLI	Blue-Green–Red	$(2R_g - R_r - R_b)/(2R_g + R_r + R_b)$	Louhaichi et al. (2001)
Green-RE(1)	Anthocyanin Reflectance Index	ARI	Green-RE	$R_g^{-1} - R_{re}^{-1}$	Gitelson et al. (2001)
Green-NIR(4)	Green NDVI	GNDVI	Green-NIR	$(R_{nir} - R_g)/(R_{nir} + R_g)$	Gitelson et al. (1996)
	Triangular Vegetation Index	TVI	Green-NIR	$0.5[120(R_{nir} - R_g) - 200(R_{nir} - R_g)]$	
	ChlorophyII Index-Green	CIG	Green-NIR	$R_{nir}/R_g - 1$	Gitelson et al. (2003)
	Triangular Greenness Index	TGI	Green-NIR	$-0.5(\lambda_r - \lambda_b)(R_r - R_g) - (\lambda_r - \lambda_g)(R_r - R_b)$	Hunt et al. (2013)
Red-RE(1)	Normalized Difference RedEdge Index	NDREI	Red-RE	$(R_{nir} - R_{re})/(R_{nir} + R_{re})$	Gitelson and Merzlyak (1994)
Red-NIR(4)	Normalized Difference Vegetation Index	NDVI	Red-NIR	$(R_{nir} - R_r)/(R_{nir} + R_r)$	Rouse et al. (1974)
	Soil Adjusted Vegetation Index	SAVI	Red-NIR	$1.5(R_{nir} - R_r)/(R_{nir} + R_r + 0.5)$	Huete (1988)
	Ratio Vegetation Index	RVI	Red-NIR	R_{nir}/R_r	Pearson and Miller (1972)
	Optimized Soil Adjusted Vegetation Index	OSAVI	Red-NIR	$1.16(R_{nir} - R_r)/(R_{nir} + R_r + 0.16)$	Rondeaux et al. (1996)
RE-NIR(1)	ChlorophyII Index-RedEdge	CIRE	RE-NIR	$R_{nir}/R_{re} - 1$	Gitelson et al. (2003)
VIS-RE-NIR(4)	Enhanced Vegetation Index	EVI	Blue-Red-NIR	$2.5(R_{nir} - R_r)/(R_{nir} + 6R_r - 7.5R_b + 1)$	Huete et al. (2002)
	Transformed ChlorophyII Absorption and Reflectance Index	TCARI	Green–Red-RE	$3[(R_{re} - R_r) - 0.2*(R_{re} - R_g)(R_{re}/R_r)]$	Haboudane et al. (2002)
	ChlorophyII Vegetation Index	CVI	Green–Red-NIR	$R_{nir}R_r/R_g^2$	Vincini et al. (2008)
	Simplified Canopy ChlorophyII Content Index	SCCCI	Red-RE-NIR	NDREI/NDVI	Raper and Varco (2015)

first calculated for each class, and their average values are chosen. Precision and Recall for a specific class are defined by

$$Precision = \frac{TP}{TP + FP}, \quad Recall = \frac{TP}{TP + FN}. \tag{3}$$

3.5. Feature ranking

It is also of great importance to identify the spectral band or SVI that has the strongest discriminating ability for yellow rust detection. In this paper, feature scoring algorithms are adopted due to its simplicity and effectiveness, which can generate a score for each feature reflecting its importance. A number of feature scoring algorithms are available according to different criteria such as Mutual Information (MI) (Cover and Thomas, 2012), Fisher score (Gu et al., 2012), ReliefF (Liu and Motoda, 2007) (see, (Roffo et al., 2017) for their comparisons by using different datasets). MI is finally adopted by trial & error experiments due to its low computational load and simple interpretation. In MI approach, statistical dependence between two random variables are measured, where a higher MI value implies a higher relevance. MI between two discrete random variables (feature quantization is generally applied to discretize continuous bands into discrete bins (Pohjalainen et al., 2015; Su et al., 2017)) Y and Z are defined by

$$MI(Y, Z) = \sum_{y \in Y} \sum_{z \in Z} p(y, z) \log\left(\frac{p(y, z)}{p(y)p(z)}\right) \tag{4}$$

where $p(y, z)$ denotes the joint probability distribution function of Y and Z, and $p(y)$ and $p(z)$ represent the marginal probability distribution functions of Y and X.

4. Results

In the section, main results of this work are presented which directly address the research objectives. It is noted that data on 23/March/2018 (inoculation) and 01/April/2018 (incubation stage) are not presented, this is because no yellow rust symptom was observed on ground and no spectral difference was found from UAV aerial image, either. Data on 17/April/2018 (after symptom onset) and 07/May/2018 (diseased stage) are presented below, since in both dates visible yellow rust symptom was observed on ground.

4.1. Data after symptom onset

Data after symptom onset is first considered, which can highlight the new challenges of UAV based remote sensing over conventional ground based monitoring approaches. Aerial images in this section were collected on 17/April/2018, 25 days after yellow rust inoculation. The camera altitude is 18 m above ground level (AGL) with a ground spatial resolution of 1.42 cm/pixel. Aerial images were processed by Pix4D, where the RGB composite of the wheat field and corresponding labelled map are displayed in Fig. 4.

4.1.1. Ground truth data
Ground truth data was collected after UAV survey as discussed in Section 3.1. Mean yellow rust severity for different wheat leaves under different levels of yellow rust inoculum is displayed in Fig. 5.

4.1.2. Spectral analysis
The mean reflectance value of original bands and different SVIs for various yellow rust infected regions is calculated in Matlab2017b and displayed in Figs. 6 and 7, respectively.

It follows from Figs. 6 and 7 that: (i) regarding both band reflectance and SVIs, there are almost no differences among different yellow rust infected regions; (ii) the subtle difference is not related to different levels of yellow rust treatment, either. It follows from Sections 4.1.1 (e.g. Figs. 5) and 4.1.2 that 25 days after yellow rust inoculation:
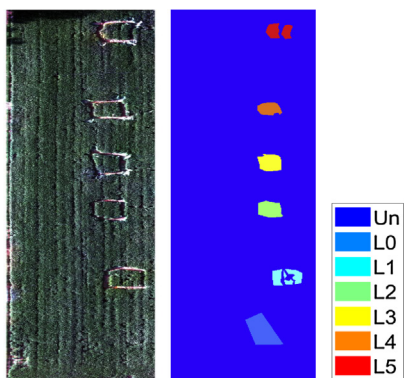
Fig. 4. Data on 17/April/2018. Left: RGB composite of wheat field with image intensity adjustment, where the small squares of 2 m× 2 m are with different levels of yellow rust inoculum; Right: labelled map including unlabelled region (Un) and six levels of yellow rust inoculum from L0-L5 with different colours, where L0 denotes healthy wheat for blank comparison. (For interpretation of the references to colour in this figure legend, the reader is referred to the web version of this article.)
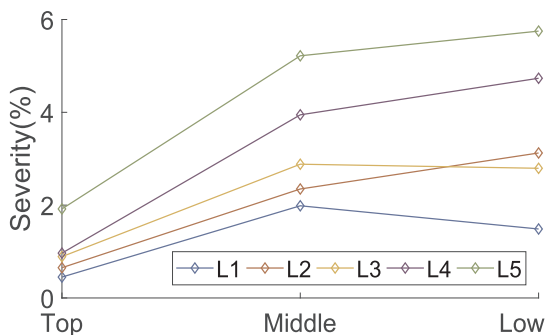

Fig. 5. Ground truth data on 17/April/2018: mean yellow rust severity for top, middle, lower leaves under various levels of yellow rust inoculum.
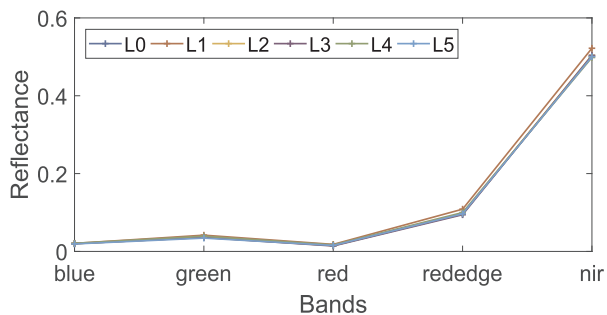
Fig. 6. Data on 17/April/2018: reflectance data of five bands under six different levels of yellow rust inoculum after symptom onset.
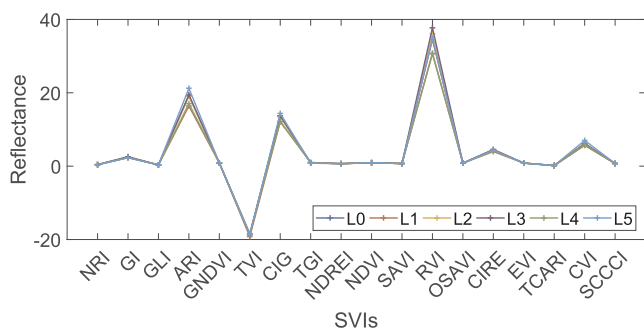

Fig. 7. Data on 17/April/2018: reflectance value of different SVIs under six levels of yellow rust inoculum after symptom onset.
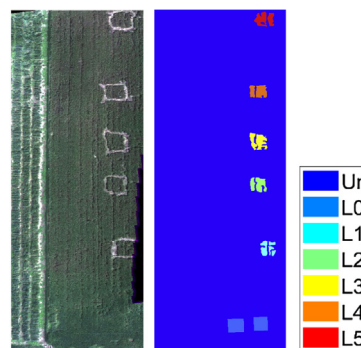

Fig. 8. Data on 07/May/2018. Left: RGB composite of the wheat field with image intensity adjustment; Right: labelled map including unlabelled region (Un) and six levels of yellow rust inoculum from L0-L5 with different colours. (For interpretation of the references to colour in this figure legend, the reader is referred to the web version of this article.)

(1) There are visible yellow rust symptoms on wheat leaf under different levels of yellow rust inoculum, where no rust symptom is observed on healthy wheat plants;
(2) Wheat yellow rust severity is positively correlated to the level of yellow rust inoculum.
(3) No reflectance differences are observed in five-band multispectral UAV image for wheat pixels under various levels of yellow rust inoculum.

4.2. Data in diseased stage

In this section, data in diseased period is further considered. Aerial images in diseased stage were collected on 07/May/2018, 45 days after yellow rust inoculation. The altitude is 16 m AGL with a ground spatial resolution of 1.07 cm/pixel. RGB composite of wheat field along with labelled map is displayed in Fig. 8.

4.2.1. Spectral analysis

Similarly, mean reflectance value of original bands and SVIs for different yellow rust infected regions is calculated and displayed in Figs. 9 and 10, respectively.

Via in-field visual inspection by experts in yellow rust research and the results in Figs. 9 and 10, it can be seen that the six levels of yellow rust infected wheat plots can be broadly divided into three classes including Healthy class (L0), Moderate (diseased) class (L2, L3 and L4) and Severe (diseased) class (L4 and L5). Consequently, the following pixel-wise classification analysis is for three classes rather than six classes (i.e. the number of different levels of yellow rust inoculum).
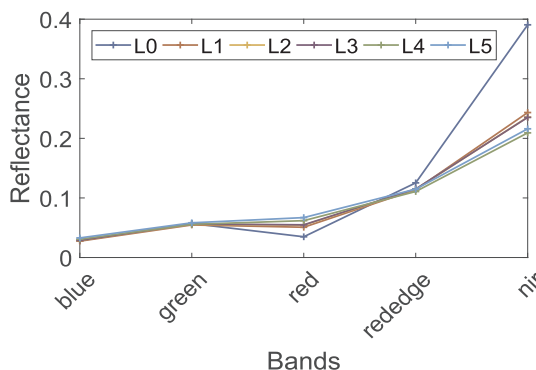

Fig. 9. Data on 07/May/2018: reflectance data of five bands under six levels of yellow rust inoculum in diseased stage.
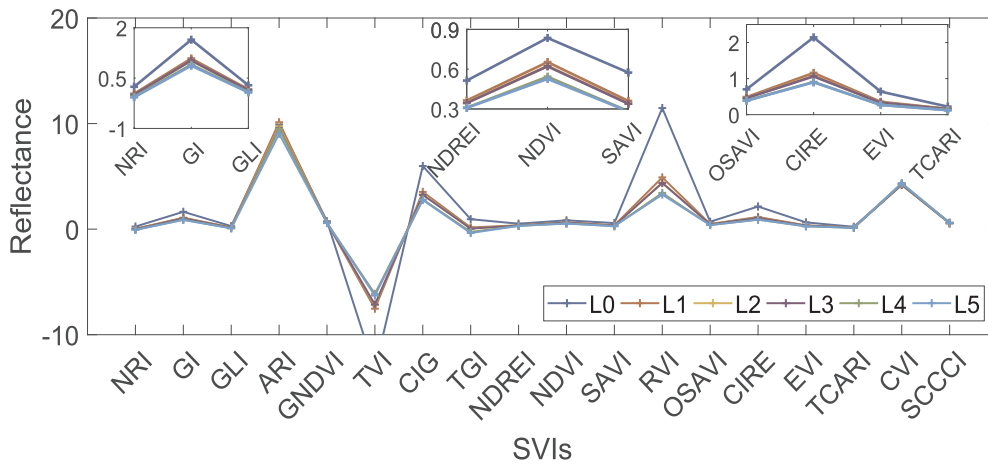
Fig. 10. Data on 07/May/2018: reflectance value of different SVIs under six levels of yellow rust inoculum in diseased stage.

4.2.2. Random forest classifier

The algorithms in this work are implemented in Matlab 2017b on Windows computer using Intel Core i7-6500U CPU@2.5 GHz with RAM 16 GB. To automatically tune the hyperparameters of random forest classifier by using Bayesian optimization, two key parameters are considered in this work including minLS and numPTS, where minLS is to control the complexity (depth) of the trees and numPTS specifies the number of predictors to sample at each node in growing the trees. In particular, $minLS \in [1, maxMinLS]$ is chosen with maxMinLS being 20 and $numPTS$ is within $[1, numF]$ with $numF$ being the number of features. In addition, tree number of random forest classifier is chosen as 150, 'AcquisitionFunctionName'is chosen 'expected-improvement-plus'and the maximum objective evaluations are chosen as 30.

In precision agriculture applications, labelled data is comparatively small. In line with this observation, only 5% (totally 16636) of all labelled pixels (totally 332751) are used for model learning (e.g. training data) and all remaining labelled pixels are used for algorithm performance evaluation. The optimized hyperparameters are $minLS = 17$ and $numPTS = 10$, where the estimated objective function values over various combinations of $minLS$ and $numPTS$ are displayed in Fig. 11. Under this parameter setting, the classification confusion matrix is displayed in Fig. 12.

In confusion matrix Fig. 12, target class denotes the ground truth while output class denotes the predicted class. The diagonal cells in green show the number/percentage of correct classification, while the off-diagonal cells show the misclassification. In particular, for Healthy class, 100648 in green is TP and 478 + 0 in red is FP, 837 + 1 in red is FN. As a result, Precision for Healthy class is 100648/(100648 + 478 + 0) = 99.5%, while Recall for Healthy class is

Fig. 12. Confusion matrix for random forest with Bayesian optimization.

100648/(100648 + 837 + 1) = 99.2%. Similarly, Precision and Recall for Moderate class and Severe class are 87.4%, 84.8%, and 80.7%, 84.7%, respectively. As a result, the average Precision and Recall for random forest classifier are 89.2% and 89.4%, respectively. The cell at the right bottom shows the overall accuracy, which is 89.3% for the optimized random forest classifier. The classification map for all labelled data is displayed in Fig. 13.
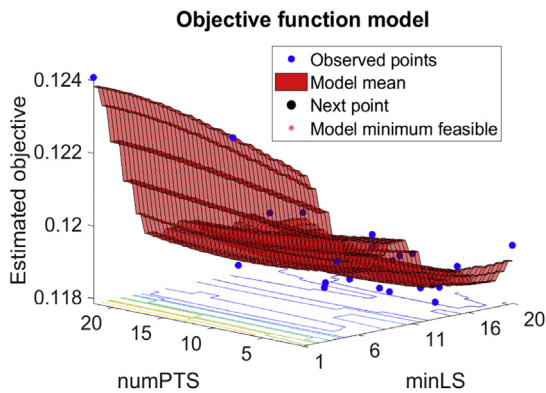

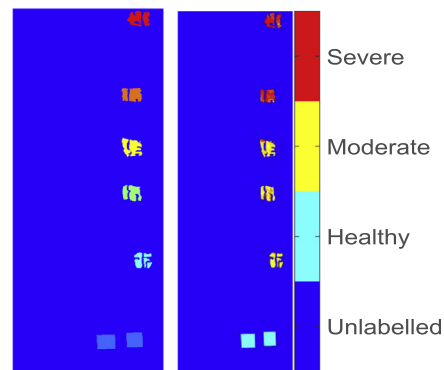**Fig. 11.** Estimated objective function values over various combinations of minLS and numPTS.

Fig. 13. Data on 07/May/2018. Left: ground truth map with Healthy class (L0), Moderate (diseased) class (L2, L3 and L4) and Severe (diseased) class (L4 and L5); Right: the classification map by the random forest classifier.
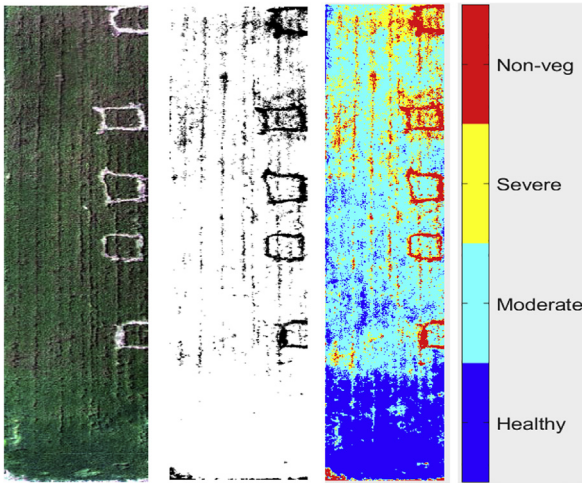
Fig. 14. Data on 07/May/2018: ROI of the experimental wheat field (left); non-vegetation segmentation using OSAVI index (middle), where black area represents non-vegetation pixels; the classification map (right).

4.2.3. Application to ROI

It follows from the left plot of Fig. 8 that yellow rust disease has spread to neighbouring wheat plants. It would be interesting to further test the developed algorithm by using the Region Of Interest (ROI) (see, left plot of Fig. 14). Considering that the ROI contains non-vegetation pixels (e.g. soil pixels), non-vegetation pixels are first segmented from wheat pixels by using the simple thresholding method (Su et al., 2018). The classical OSAVI (Rondeaux et al., 1996) is adopted in this work, where the threshold is chosen 0.36. The ROI, non-vegetation segmentation result and classification map by the developed system is displayed in Fig. 14. Very promising results have been obtained by comparing RGB composite map (along with in-field visual inspection) of ROI and classification map.

4.3. SVI ranking

In order to evaluate the discriminating capability of each band and SVI in yellow rust detection, MI based feature ranking is adopted, where MI value between each band/SVI and yellow rust class label is calculated and plotted in Fig. 15.

It follows from Fig. 15 that different bands or SVIs have different yellow rust discriminating abilities. The ordered bands and SVIs for yellow rust detection are RVI, NDVI, OSAVI, GI, NRI, SAVI, GLI, EVI, TGI, CIRE, NDREI, CIG, GNDVI, TVI, NIR, RED, TCARI, SCCCI, RedEdge, Blue, ARI, Green, CVI. In particular, the top three SVIs for
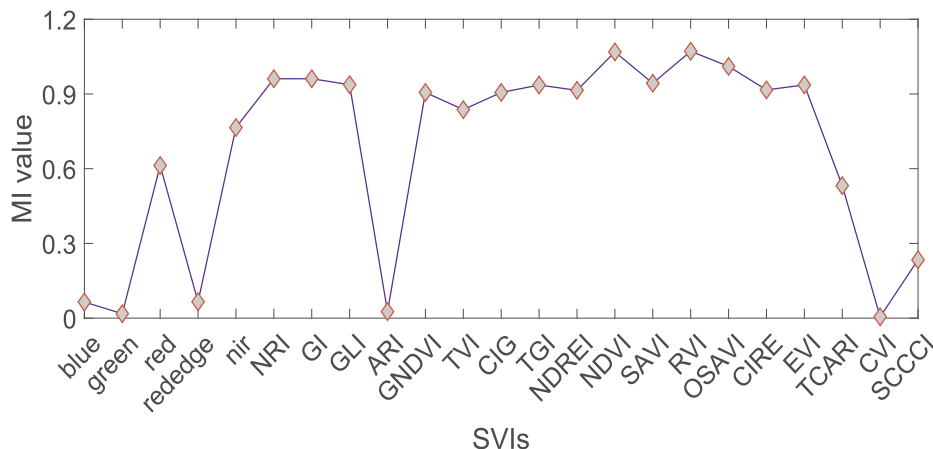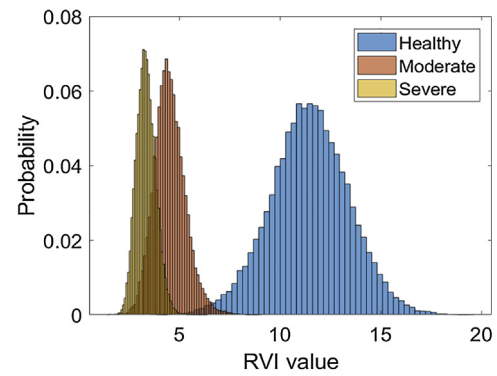

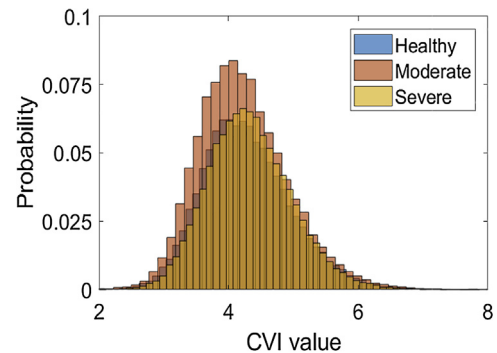**Fig. 16.** RVI probability histogram under different yellow rust classes.

Fig. 17. CVI probability histogram under different yellow rust classes.

separating healthy and yellow rust infected wheat plants are RVI, NDVI and OSAVI; while the top two spectral bands are NIR and Red.

To visually see the discriminating ability of different SVIs in yellow rust detection, the probability histogram of the best SVI (i.e. RVI) and worst SVI (i.e. CVI) under different yellow rust severities is displayed in Figs. 16 and 17, respectively. It can be easily seen that RVI has a much better discriminating ability than CVI, since CVI distributions under Healthy class, Moderate class and Severe class have too much overlap.

5. Discussions

Yellow rust detection/quantification plays a vital role for sustainable agriculture, where in-season spatial distribution of yellow rust infection and severity assessment enables the site-specific disease treatment and management, increasing yield, reducing economic burden and environmental pollution (Sankaran et al., 2010). Yellow

Fig. 15. MI quantifying the usefulness of each band/SVI, where a higher MI value implies a strong yellow rust discriminating ability.

rust disease usually brings certain changes in crop vigour, pigments, ChlorophyII and water stress, and consequently alters crop spectral reflectance (Franke et al., 2005). Therefore, indirect detection/quantification of yellow rust by using spectral reflectance extracted from multispectral or hyperspectral camera is promising and attracting increasing research interests due to the substantially reduced labour involved and potential for applications at farmland scales.

Conventional studies are mainly focused on leaf-level yellow rust detection by using hyperspectral images (Moshou et al., 2004; Franke et al., 2005; Ashourloo et al., 2014). These studies are very useful in identifying the sensitive narrow bands and SVIs for yellow rust detection. For example, 543 nm, 630 nm, 750 nm and 861 nm were identified to be useful wavelengths for yellow rust detection in Moshou et al. (2004). In addition, NDVI, GI, ARI were identified to be best SVIs among 22 narrow-band SVIs in Ashourloo et al. (2014). It should also be noted that there also exist substantial differences between leaf (on ground) level and UAV remote sensing in yellow rust detection. For example, spectral reflectance differences between healthy leaf and yellow rust infected leaf can be detected in inoculation stage in Franke et al. (2005) and Wang et al. (2016), which is very hard for remote sensing multispectral image even though state-of-the-art multispectral camera (RedEdge) is deployed at a very low altitude of 16 m in this work (see, Section 4.1). The key challenges of remote sensing for disease monitoring in comparison to ground based approach is the substantially reduced spatial resolution in addition to other factors (e.g. atmosphere, illumination variation) affecting crop reflectance. Consequently, there is an urgent need of remote sensing study for yellow rust detection at farmland scales, which was rarely performed in the existing literature.

With the advert of easily-deployed UAV and small-size cameras of light weight, low price and high resolution, UAV based remote sensing is gathering ever-increasing research interests and has become an important complement to satellite and manned-aircraft remote sensing in crop stress (e.g. disease, pest, drought and nitrogen) monitoring (Zhang and Kovacs, 2012) due to its user-defined spatial, spectral and temporal resolutions and suitability for small or middle scale farmlands. For example, RGB and thermal camera are put on a UAV for rice lodging assessment in Liu et al. (2018) by exploiting color, texture and temperature information. Four-band multispectral Sequoia camera was installed on an UAV in Romero et al. (2018) for vineyard water status estimation by using Artificial Neural Network. Following this line of thought, in this work the potential of low-cost, high-resolution five-band multispectral camera (RedEdge) and a low-altitude airborne platform is exploited for winter wheat yellow rust detection/quantification. In comparison with conventional studies in Liu et al. (2018) and Romero et al. (2018), the five-band RedEdge camera not only possesses more spectral information but also a higher spatial resolution. Necessary materials for this study were provided by in-field experiment design (i.e. six levels of yellow rust inoculum), aerial image acquisition of different yellow rust developmental stages and ground data truthing by visual inspection.

Spectral reflectance analysis for aerial imagery at early onset of symptom along with ground truth severity data implies that visible yellow rust symptoms on wheat leaf can be observed 25 days after inoculation, however, no obvious spectral differences are observed between healthy wheat and wheat infected by different levels of yellow rust inoculum, where the spatial ground resolution of the five-band multispectral imagery is 1.42 cm. This is mainly due to the under-development of the disease and low (compared with ground level data) spatial resolution.

Spectral reflectance analysis and pixel-wise random forest classification (with hyperparameters being automatically tuned by Bayesian optimization) are performed on data in diseased stage. Experimental results indicate that

(i) Significant differences are observed in spectral reflectance among

healthy wheat plants and wheat plants infected by various levels of yellow rust inoculum;

(ii) By dividing the data into Healthy class, Moderate (diseased) class and Severe (diseased) class, the developed yellow rust monitoring system by using random forest classifier and band/SVI features can achieve promising classification performance with average Precision, Recall and Accuracy being 89.2%, 89.4% and 89.3%, respectively;

(iii) It is also discovered by mutual information based feature ranking that different spectral bands and SVIs have different yellow rust discriminating abilities. In particular, the top three SVIs for yellow rust detection are RVI, NDVI and OSAVI, while ARI and CVI have poor discriminating ability. The top band is NIR followed by Red, while RedEdge, Blue and Green have poor discriminating ability. Our results are different from leaf yellow rust (Ashourloo et al., 2014), although NDVI is identified to be very useful SVI in both studies, our results indicate that ARI is almost useless. In comparison to the result in Moshou et al. (2004), our results indicate that Green reflectance provides little yellow rust discriminating information.

Although the results are very positive, there are still room for further improvement, which are summarized in the following aspects.

(i) Identify the best band and SVI combination to build a better (in terms of simplicity, accuracy, etc.) classification model by using advanced dimension reduction approaches (Roffo et al., 2017);

(ii) Design more levels of yellow rust infection or combining the data of different disease developmental stages so that regression analysis can be performed between SVIs and disease severity in a quantitative manner (Liu et al., 2018).

6. Conclusions

This work aims at exploiting the potentials of low-cost five-band multispectral camera (RedEdge), low-altitude airborne platform and state-of-the-art machine learning techniques in the automatic detection of winter wheat stress caused by yellow rust. An automated yellow rust monitoring system is developed by learning from labelled UAV aerial multispectral image, which is user-friendly, low-cost and suitable for use at farmland scales. An experiment was designed for system validation by infecting winter wheat with various levels of yellow rust inoculum, where aerial multispectral images under different yellow rust developmental stages were also captured by an Unmanned Aerial Vehicle at an altitude of 16–24 m with a ground resolution of 1–1.5 cm/pixel. Experimental results show that the developed system by using optimized random forest classifier can achieve good classification performance with an average Precision, Recall and Accuracy of 89.2%, 89.4% and 89.3% respectively when yellow rust is in diseased stage. The spectral band and spectral vegetation index (SVI) with a strong discriminating capability are also identified by using mutual information based feature ranking. In particular, the top three SVIs for separating healthy and yellow rust infected wheat plants are RVI, NDVI and OSAVI; while the top two spectral bands are NIR and Red. The learnt system is also applied to the whole farmland of interest with a promising result.

Contributions

Overall research idea (Wen-Hua Chen, Cunjia Liu and Lei Guo); Experiment design (Cunjia Liu, Xiaoping Hu, Xiangming Xu, Wen-Hua Chen and Jinya Su); UAV-Camera system (Matthew Coombes, Cunjia Liu and Jinya Su); Ground data collection (Xiaoping Hu, Conghao Wang); Data processing and algorithm design (Jinya Su); Paper writing (Jinya Su, Wen-Hua Chen, Xiangming Xu), Coordination (Qingdong Li, Lei Guo, Xiangming Xu, Cunjia Liu and Jinya Su).

Acknowledgements

This work was supported by Science and Technology Facilities Council (STFC) under Newton fund with Grant No. ST/N006852/1. Xi'an Tongfei Aviation Technology Co., Ltd was also acknowledged for their professional support in flying UAV for data collection.

References

Ashourloo, D., Mobasheri, M.R., Huete, A., 2014. Evaluating the effect of different wheat rust disease symptoms on vegetation indices using hyperspectral measurements. Remote Sens. 6 (6), 5107–5123.

Ballester, C., Hornbuckle, J., Brinkhoff, J., Smith, J., Quayle, W., 2017. Assessment of in-season cotton nitrogen status and lint yield prediction from unmanned aerial system imagery. Remote Sens. 9 (11), 1149.

Bellvert, J., Zarco-Tejada, P., Girona, J., Fereres, E., 2014. Mapping crop water stress index in a pinot-noirvineyard: comparing ground measurements with thermal remote sensing imagery from an unmanned aerial vehicle. Precision Agric. 15 (4), 361–376.

Cover, T.M., Thomas, J.A., 2012. Elements of Information Theory. John Wiley & Sons.

Devadas, R., Lamb, D., Simpfendorfer, S., Backhouse, D., 2009. Evaluating ten spectral vegetation indices for identifying rust infection in individual wheat leaves. Precision Agric. 10 (6), 459–470.

Filella, I., Serrano, L., Serra, J., Penuelas, J., 1995. Evaluating wheat nitrogen status with canopy reflectance indices and discriminant analysis. Crop Sci. 35 (5), 1400–1405.

Franke, J., Menz, G., Oerke, E.-C., Rascher, U., 2005. Comparison of multi-and hyper-spectral imaging data of leaf rust infected wheat plants. In: Remote Sensing for Agriculture, Ecosystems, and Hydrology VII, vol. 5976. International Society for Optics and Photonics, pp. 59761D.

Gitelson, A., Merzlyak, M.N., 1994. Quantitative estimation of chlorophyll-a using re-flectance spectra: Experiments with autumn chestnut and maple leaves. J. Photochem. Photobiol., B 22 (3), 247–252.

Gitelson, A.A., Kaufman, Y.J., Merzlyak, M.N., 1996. Use of a green channel in remote sensing of global vegetation from eos-modis. Remote Sens. Environ. 58 (3), 289–298.

Gitelson, A.A., Merzlyak, M.N., Chivkunova, O.B., 2001. Optical properties and non-destructive estimation of anthocyanin content in plant leaves. Photochem. Photobiol. 74 (1), 38–45.

Gitelson, A.A., Gritz, Y., Merzlyak, M.N., 2003. Relationships between leaf chlorophyll content and spectral reflectance and algorithms for non-destructive chlorophyll as-sessment in higher plant leaves. J. Plant Physiol. 160 (3), 271–282.

Gu, Q., Li, Z., Han, J., 2012. Generalized fisher score for feature selection, arXiv preprint arXiv:1202.3725.

Haboudane, D., Miller, J.R., Tremblay, N., Zarco-Tejada, P.J., Dextraze, L., 2002. Integrated narrow-band vegetation indices for prediction of crop chlorophyll content for application to precision agriculture. Remote Sens. Environ. 81 (2-3), 416–426.

Ho, T.K., 1995. Random decision forests. In: Document Analysis and Recognition, 1995. Proceedings of the Third International Conference on, vol. 1. IEEE, pp. 278–282.

Ho, T.K., 1998. The random subspace method for constructing decision forests. IEEE Trans. Pattern Anal. Mach. Intell. 20 (8), 832–844.

Huang, W., Lamb, D.W., Niu, Z., Zhang, Y., Liu, L., Wang, J., 2007. Identification of yellow rust in wheat using in-situ spectral reflectance measurements and airborne hyperspectral imaging. Precision Agric. 8 (4-5), 187–197.

Huang, W., Guan, Q., Luo, J., Zhang, J., Zhao, J., Liang, D., Huang, L., Zhang, D., 2014. New optimized spectral indices for identifying and monitoring winter wheat diseases. IEEE J. Sel. Top. Appl. Earth Observat. Remote Sens. 7 (6), 2516–2524.

Huete, A.R., 1988. A soil-adjusted vegetation index (savi). Remote Sens. Environ. 25 (3), 295–309.

Huete, A., Didan, K., Miura, T., Rodriguez, E.P., Gao, X., Ferreira, L.G., 2002. Overview of the radiometric and biophysical performance of the modis vegetation indices. Remote Sens. Environ. 83 (1-2), 195–213.

Hunt Jr., E.R., Doraiswamy, P.C., McMurtrey, J.E., Daughtry, C.S., Perry, E.M., Akhmedov, B., 2013. A visible band index for remote sensing leaf chlorophyll content at the canopy scale. Int. J. Appl. Earth Obs. Geoinf. 21, 103–112.

Jin, X., Liu, S., Baret, F., Hemerlé, M., Comar, A., 2017. Estimates of plant density of wheat crops at emergence from very low altitude uav imagery. Remote Sens. Environ. 198, 105–114.

Liu, H., Motoda, H., 2007. Computational Methods of Feature Selection. CRC Press.

Liu, T., Li, R., Zhong, X., Jiang, M., Jin, X., Zhou, P., Liu, S., Sun, C., Guo, W., 2018. Estimates of rice lodging using indices derived from uav visible and thermal infrared images. Agric. For. Meteorol. 252, 144–154.

Liu, W., Yang, G., Xu, F., Qiao, H., Fan, J., Song, Y., Zhou, Y., 2018. Comparisons of detection of wheat stripe rust using hyperspectral and uav aerial photography. Acta Phytopathol. Sinica 48 (2), 223–227.

López, M.M., Bertolini, E., Olmos, A., Caruso, P., Gorris, M.T., Llop, P., Penyalver, R., Cambra, M., 2003. Innovative tools for detection of plant pathogenic viruses and bacteria. Int. Microbiol. 6 (4), 233–243.

Louhaichi, M., Borman, M.M., Johnson, D.E., 2001. Spatially located platform and aerial photography for documentation of grazing impacts on wheat. Geocarto Int. 16 (1), 65–70.

Moshou, D., Bravo, C., West, J., Wahlen, S., McCartney, A., Ramon, H., 2004. Automatic detection of yellow rustin wheat using reflectance measurements and neural net-works. Comput. Electron. Agric. 44 (3), 173–188.

Pavli, O.I., Stevanato, P., Biancardi, E., Skaracis, G.N., 2011. Achievements and prospects in breeding for rhizomania resistance in sugar beet. Field Crops Res. 122 (3), 165–172.

Pearson, R.L., Miller, L.D., 1972. Remote mapping of standing crop biomass for estima-tion of the productivity of the shortgrass prairie. In: Remote Sensing of Environment, VIII, p. 1355.

Pohjalainen, J., Räsänen, O., Kadioglu, S., 2015. Feature selection methods and their combinations in high-dimensional classification of speaker likability, intelligibility and personality traits. Comput. Speech Lang. 29 (1), 145–171.

Raper, T., Varco, J., 2015. Canopy-scale wavelength and vegetative index sensitivities to cotton growth parameters and nitrogen status. Precision Agric. 16 (1), 62–76.

Roffo, G., Melzi, S., Castellani, U., Vinciarelli, A., 2017. Infinite latent feature selection: A probabilistic latent graph-based ranking approach, arXiv preprint arXiv:1707.07538.

Romero, M., Luo, Y., Su, B., Fuentes, S., 2018. Vineyard water status estimation using multispectral imagery from an UAV platform and machine learning algorithms for irrigation scheduling management. Comput. Electron. Agric. 147, 109–117.

Rondeaux, G., Steven, M., Baret, F., 1996. Optimization of soil-adjusted vegetation in-dices. Remote Sens. Environ. 55 (2), 95–107.

Rouse Jr J., Haas, R., Schell, J., Deering, D., 1974. Monitoring vegetation systems in the great plains with erts.

Sankaran, S., Mishra, A., Ehsani, R., Davis, C., 2010. A review of advanced techniques for detecting plant diseases. Comput. Electron. Agric. 72 (1), 1–13.

Snoek, J., Larochelle, H., Adams, R.P., 2012. Practical bayesian optimization of machine learning algorithms. In: Advances in Neural Information Processing Systems, pp. 2951–2959.

Su, J., Yi, D., Liu, C., Guo, L., Chen, W.-H., 2017. Dimension reduction aided hyper-spectral image classification with a small-sized training dataset: experimental com-parisons. Sensors 17 (12), 2726.

Su, J., Coombes, M., Liu, C., Guo, L., Fang, S., Chen, W.-H., 2018. Machine learning based crop drought mapping system by uav remote sensing imagery. Unmanned Syst.

Su, J., Coombes, M., Liu, C., Guo, L., Chen, W.-H., 2018. Wheat drought assessment by remote sensing imagery using unmanned aerial vehicle. In: Chinese Control Conference, the 37th. IEEE.

Thornton, C., Hutter, F., Hoos, H.H., Leyton-Brown, K., 2013. Auto-weka: Combined se-lection and hyperparameter optimization of classification algorithms. In: Proceedings of the 19th ACM SIGKDD International Conference on Knowledge Discovery and Data Mining. ACM, pp. 847–855.

Tucker, C.J., 1979. Red and photographic infrared linear combinations for monitoring vegetation. Remote Sens. Environ. 8 (2), 127–150.

Vincini, M., Frazzi, E., D'Alessio, P., 2008. A broad-band leaf chlorophyll vegetation index at the canopy scale. Precision Agric. 9 (5), 303–319.

Wang, H., Qin, F., Ruan, L., Wang, R., Liu, Q., Ma, Z., Li, X., Cheng, P., Wang, H., 2016. Identification and severity determination of wheat stripe rust and wheat leaf rust based on hyperspectral data acquired using a black-paper-based measuring method. PloS One 11 (4), e0154648.

Yi, D., Su, J., Liu, C., Chen, W.-H., 2017. Personalized driver workload inference by learning from vehicle related measurements. IEEE Trans. Syst. Man Cybernet.: Syst.

Yuan, L., Huang, Y., Loraamm, R.W., Nie, C., Wang, J., Zhang, J., 2014. Spectral analysis of winter wheat leaves for detection and differentiation of diseases and insects. Field Crops Res. 156, 199–207.

Yuan, L., Zhang, H., Zhang, Y., Xing, C., Bao, Z., 2017. Feasibility assessment of multi-spectral satellite sensors in monitoring and discriminating wheat diseases and insects. Optik-Int. J. Light Electron Opt. 131, 598–608.

Yue, J., Yang, G., Li, C., Li, Z., Wang, Y., Feng, H., Xu, B., 2017. Estimation of winter wheat above-ground biomass using unmanned aerial vehicle-based snapshot hyper-spectral sensor and crop height improved models. Remote Sens. 9 (7), 708.

Zarco-Tejada, P.J., Berjón, A., López-Lozano, R., Miller, J.R., Martín, P., Cachorro, V., González, M., De Frutos, A., 2005. Assessing vineyard condition with hyperspectral indices: Leaf and canopy reflectance simulation in a row-structured discontinuous canopy. Remote Sens. Environ. 99 (3), 271–287.

Zhang, C., Kovacs, J.M., 2012. The application of small unmanned aerial systems for precision agriculture: a review. Precis. Agric. 13 (6), 693–712.

Zhang, J., Huang, W., Li, J., Yang, G., Luo, J., Gu, X., Wang, J., 2011. Development, evaluation and application of a spectral knowledge base to detect yellow rust in winter wheat. Precision Agric. 12 (5), 716–731.

Zhang, J., Pu, R., Huang, W., Yuan, L., Luo, J., Wang, J., 2012. Using in-situ hyperspectral data for detecting and discriminating yellow rust disease from nutrient stresses. Field Crops Res. 134, 165–174.

Zhang, J., Pu, R., Loraamm, R.W., Yang, G., Wang, J., et al., 2014. Comparison between wavelet spectral features and conventional spectral features in detecting yellow rust for winter wheat. Comput. Electron. Agric. 100, 79–87.